Nonlinear optical specifications of the Mathieu quantum dot with screw dislocation

Mustafa Kemal Bahar[a], **Pınar Başer**[b]

Department of Physics, Faculty of Science, Sivas Cumhuriyet University, 58140 Sivas, Turkey

Abstract In this study, the nonlinear optical properties of screw dislocation $In_xGa_{1-x}As/GaAs$ Mathieu quantum dots (MQDs) are theoretically investigated for the first time, focusing on the optical rectification (NOR), second harmonic generation (SHG), and third harmonic generation (THG). In addition to the screw dislocation in the structure, external electric and magnetic fields, as well as the Aharonov–Bohm (AB) flux, are applied to the system. The aim of the study is to interpret how the characteristics of the NOR, SHG, and THG of MQDs change depending on the screw dislocation defect, external fields, AB flux, and structural factors such as indium concentration (*In*) and quantum dot width. The wave equation of the system is solved using the effective mass approximation and the Runge–Kutta–Fehlberg method in cylindrical coordinates, taking into account the direction of twist and the symmetry of the structure. The influence of all parameters on the nonlinear optical properties of the MQD with screw dislocation and their alternatives are discussed in detail. Furthermore, the optimality of the structure is discussed for a certain amount of screw dislocation, which can be important for experimental applications and device designs.

1 Introduction

Developing microfabrication methods have allowed the fabrication of low-dimensional structures and nanostructures in semiconductors where quantum confinement effects occur [1]. One of these low-dimensional systems in semiconductors is the quantum dots, which have atom-like, Dirac delta-functional state density, in which the carriers are surrounded in three dimensions [2]. Therefore, these structures are also called "artificial atoms." Quantum dots are used in the design of many optoelectronic devices such as memory chips [3], quantum computing [4], quantum dot lasers [5], photovoltaic devices [6], quantum dot displays [7] and photocatalysts [8]. Additionally, due to their small sizes, some quantum dots (QDs) can be suspended in a solution, which allows for their utilization in inkjet printing and spin coating applications [9]. Nonlinear optics is the study of phenomena that arise from the alteration of the optical properties of a material as a result of the interaction with photons [10]. In nonlinear optical phenomena, the response of a material to an applied optical field depends nonlinearly on the strength of the optical field. The SHG, which is a nonlinear optical phenomenon, occurs as a result of the portion of the atomic response that scales quadratically with the strength of the applied optical field. As a result, the intensity of the light generated at the second harmonic frequency tends to increase as the square of the intensity of the applied laser light [11]. The SHG processes have an activity in nonlinear optoelectronic devices, optical switching devices and optical communication. In addition, low-dimensional semiconductor systems are becoming more and more important day by day in parallel with the advancement of technology, due to the need for circuit components containing high mobility carriers in order for advanced functional devices to operate at an optimum level. Therefore, the nonlinear optical properties of low-dimensional semiconductor materials have become more interesting [12–14]. The MQD, due to its confinement potential, creates a parabolic confinement on electrons. This aligns with the condition suggested by some experimental studies that the most suitable quantum dot profiles for confining electrons should have a well-like structure [15, 16]. The quantum dot including the Mathieu potential confinement [17], which can be produced with advanced nanofabrication technology, will be an important guide for new device designs and optimization. In this study, the MQD including the screw dislocation, consisting of GaInAs/InAs, is taken into consideration. GaInAs ternary semiconductor compound has some advantages compared to other semiconductor compounds in electronics and optoelectronics [18]. Some of the application areas of the GaInAs semiconductor compound include lasers, infrared photodetectors, avalanche photodiodes, photovoltaics and transistors [19–22]. Quantum dot lasers obtained from this semiconductor are more advantageous than quantum well lasers in terms of emitting at a wavelength of 1.3 mm. This emission wavelength falls within the telecommunications wavelength range. Additionally, GaInAs/(Al)GaAs quantum dot lasers have high power applications at shorter wavelengths for rare-earth lasers and fiber amplifiers [19]. In addition, quantum dot infrared photodetectors (QDIP) are

[a] e-mail: mussiv58@gmail.com (corresponding author)

[b] e-mail: pbaser34@gmail.com

more advantageous than quantum well infrared detectors (QWIP) in terms of variable state density, longer lifetime of charge carriers, high operating temperature and low dark current [20]. It is evident that the GaInAs/(Al)GaAs heterostructure has numerous applications in the energy, information industry, and communication fields, providing technical advantages such as high mobility and wide communication bandwidth [21–24].

The Aharonov–Bohm effect is a quantum mechanical phenomenon in which an electrically charged particle is under the influence of an electromagnetic potential (ϕ, A) [25]. The Aharonov–Bohm effect is the phase shift that occurs in the wave function of a charged particle passing around a long solenoid, despite the magnetic field inside the solenoid and the wave function of the particle being negligible in the region it passes through. This phase shift is a result of the enclosed magnetic field. This phase shift has also been confirmed experimentally. In electromagnetism, it can be observed that the rotation of the electric field and the divergence of the magnetic field are both zero. Therefore, an electrostatic field can be defined as the gradient of a scalar, and a magnetic field can be defined as the curl of a vector potential. One of the important outcomes of the Aharonov–Bohm effect is that it explains whether potentials are "physical" or a suitable tool for calculating force fields [26]. Many studies have been carried out investigating the effect of the Aharonov–Bohm (AB) flux field as well as the external magnetic field on electronic and optical properties in low-dimensional structures [27–30]. The effect of the magnetic and Aharonov–Bohm (AB) flux fields of a cylindrical quantum dot system on both in-band and inter-band transitions in consideration of two-photon absorption has been investigated. The increase in the magnetic field causes a blueshift in the spectrum for both in-band and inter-band transitions, while the change in the AB flux field affects only the inter-band transitions [31]. It has been demonstrated that the formation of high harmonics in carbon nanotubes can be efficiently controlled using the Aharonov–Bohm effect when a static magnetic field is applied along the carbon nanotube. In particular, when a magnetic field is applied to metallic carbon nanotubes, which can be considered as one-dimensional massless Dirac systems, the appropriate values of the magnetic field lead to nonzero gaps in the THz regime. When gapped Dirac systems are obtained from gapless Dirac systems, a significant increase in the intensity of high-harmonic generation in the THz range is observed. A method has been found to manipulate high-harmonic generation in nanotubes using magnetic fields and Aharonov–Bohm fields [32]. The external electric field, magnetic field, and AB flux field applied to low-dimensional structures lead to significant results on optical and electronic properties as they modify the symmetry of the structure and the profile of the effective confinement potential [33–36]. Therefore, by considering these fields as arguments, a functional tuning mechanism can be established on the optical and electronic properties, which forms an important basis for new device designs. Additionally, as expected, variations in structural parameters such as potential depth and potential width also have an impact on electronic and optical properties. In this study, the effects of structural influences on the nonlinear optical properties of MQDs are investigated in detail, in addition to the external fields.

Crystals can acquire defects both during growth and due to external factors, and these defects have effects on the physical and mechanical properties of materials. Some of these defects are named based on their geometry and the deformations they cause, such as screw or spiral dislocations. Some dislocations are intentionally created for a specific purpose. In this study, the effect of screw dislocation, which is a two-dimensional linear defect, on the electronic and optical properties of the MQD is considered. Screw dislocation occurs as a result of the twisting of a crystal, leading to a spiral inclination of an atomic plane (see Fig. 1). The direction and magnitude of the torsion are characterized by the Burgers vector of the dislocation (see Fig. 1). Screw dislocation defect forms a stress in the structure by changing the continuity of the semiconductor crystal medium. When the repulsive scalar potential resulting from the lattice deformation is included in the interaction potential energy, it is expected to change the electronic and optical properties considerably [37, 38]. One of the methods of inspecting the effect of deformation potential on electron movement is perturbation theory. The stress contribution is added to the Schrödinger equation as a perturbation term, and its effect on the particle is examined [39, 40]. Another method is ion displacement, which causes a change in the volume of the Wigner–Seitz cell, resulting in a change in the energy of a zero wave vector electron. This is evaluated within the framework of deformation potential
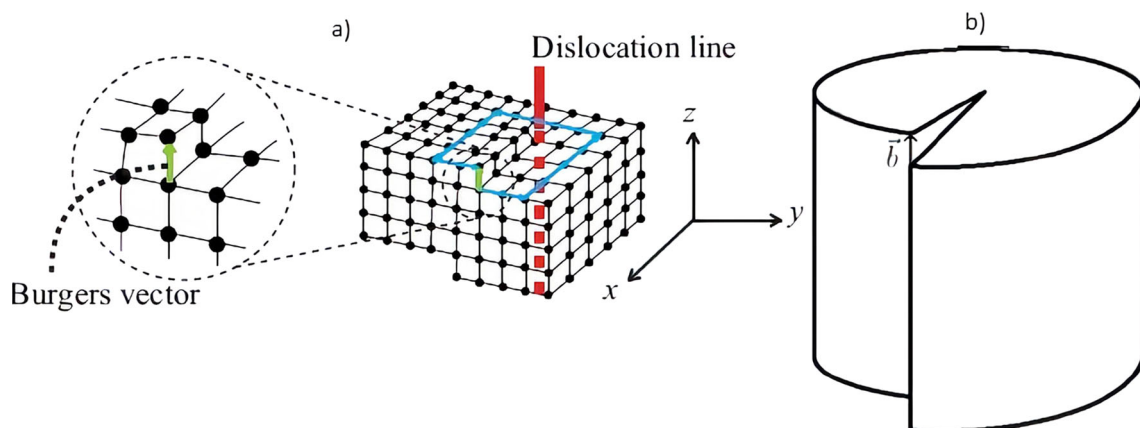
Fig. 1 a Three-dimensional lattice including a screw dislocation, within the dislocation line and Burgers vector [52], **b** screw dislocation scheme in the 3D cylindrical bulk crystal [57, 58]

theory [41, 42]. Screw dislocations in a crystal create an effective potential field, leading to high current leakage and low breakdown voltage. Therefore, it is well-known that they can significantly impair device performance [43]. In addition, it has been determined that the deformation potential arising from the stress caused by the dislocation reduces the photoluminescence strength as a result of the modification of the state density [44]. The effect of the screw dislocation on the energy levels, direct inter-band absorption coefficient and threshold frequency of non-relativistic electrons on a two-dimensional solid within the Kratzer potential under an external magnetic field and Aharonov–Bohm (AB) field has been viewed [45]. In these mentioned studies, the significant physical effects of the screw dislocation on crystals and combined systems have provided an important motivation for examining the relevant effect on the optical and electronic properties of InGaAs/GaAs MQD. In light of the fact that nonlinear optical processes play an effective role in many optoelectronic device designs, it can be said that nonlinear optical rectification (NOR), second harmonic generation (SHG), and third harmonic generation (THG) are among the most notable processes. The effect of external electric and magnetic fields applied to low-dimensional structures on the structural symmetry, as well as the ability to intentionally manipulate this effect, enables the targeted control of both electronic and nonlinear optical properties [46–49]. In this work, the effect of screw dislocation on the nonlinear optical properties of MQD has been investigated, including external electric field, magnetic field, and AB flux field. Additionally, the influence of structural parameters such as quantum dot depth and width on the electronic and optical properties has been examined. From an application standpoint, it is important to determine the optimum conditions by manipulating the external fields and adjusting the structural parameters. Similarly, minimizing the undesired effects of screw dislocation on the optical properties of MQD by intentionally applying external fields would be beneficial in practical applications. The presence of screw dislocation can also be determined for very specific purposes and at what level it should be maintained. In this context, the main motivation of the study is to explain and control the effect mechanism of screw dislocation deformation, the effects of electric field, external magnetic field, and AB flux field, and to determine the alternatives between these relevant factors on the NOR, SHG, and THG. The obtained results provide a manual-like guidance for the combined MQD system considered, which can be valuable in experimental applications.

The work is organized as follows: Section 2 presents the theoretical calculation procedure. In Sect. 3, the evaluations on the electronic and nonlinear optical specifications are carried out, and finally in Sect. 4, the results obtained are outlined.

2 Theoretical model and procedure

The relevant system metric for moving electrons in a three-dimensional crystal under the influence of single screw dislocation ($\mathbf{b} = b\mathbf{e_z}$ Burgers vector) along z-axis is expressed in cylindrical coordinates as [50]

$$ds^2 = dr^2 + r^2 d\phi^2 + (dz + \beta d\phi)^2, \tag{1}$$

with $(r, \phi, z) \rightarrow (r, \phi + 2\pi, z)$ and $\beta = b/2\pi$. The effective vector potential caused by dislocation in the crystal is analyzed employing the continuum limit approach within the framework of the tight-binding model of a discrete lattice with dislocation [51]. In this case, the tight-binding Hamiltonian is given by

$$H = -\frac{1}{2} \sum_{\mathbf{n},\mathbf{a(n)}} t[\mathbf{a(n)}](c^\dagger[\mathbf{n} + \mathbf{a(n)}]c[\mathbf{n}] + c^\dagger[n]c[\mathbf{n} + \mathbf{a(n)}]), \tag{2}$$

with $\mathbf{n}$ (the position vector at a lattice section), $\mathbf{a(n)}$ (the bond vector end from $\mathbf{n}$ to nearest neighbor sections), $t[\mathbf{a(n)}]$ (the transfer energy along $\mathbf{a(n)}$), $c^\dagger$ and c (creation and annihilation operators which in turn enable $[c((\mathbf{n})), c^\dagger(\mathbf{m})] = (1/|(\mathbf{a})|^3)\delta_{\mathbf{n},\mathbf{m}}$). In consideration of the continuous approach of the tight-binding Hamiltonian, $c[\mathbf{n} + \mathbf{a(n)}]$ is expanded to second order in the lattice constant $\mathbf{a}$, and the modulation in $t[\mathbf{a(n)}]$ is also taken into consideration [52]. In this case, a potential term arises from structural distortion, which affects the electronic, optical and statistical properties of the structure in terms of carriers in the semiconductor [53]. This potential can be evaluated as "deformed potential," stating as, being $m^\star$ is the effective mass of electron, a is the lattice constant ($a = 0.054a_0$),

$$V_{sd}(r) = \frac{\hbar^2}{2m^\star a^2} \frac{b^2}{4\pi^2 r^2} \left(2 + a^2 \left(\frac{\partial}{\partial z}\right)^2\right). \tag{3}$$

The effective mass approximation is used as a crucial tool in understanding the behavior of charge carriers in solid-state physics. This approach allows us to consider charge carriers, such as electrons and holes, moving under the influence of the periodic potential energy within the crystal structure, as if they were free particles. By simplifying the complex quantum mechanical interactions within the crystal lattice and accounting for certain crystal defects, the effective mass approximation facilitates the analysis of charge carriers' behavior in the energy band structure. It plays a vital role, especially in comprehending the electrical and optical properties of semiconductor materials. In the design and analysis of semiconductor devices, the effective mass approximation is utilized to calculate fundamental parameters like charge carrier mobility, transport velocity, carrier effectiveness, and recombination rates. Moreover, it significantly contributes to the development of optoelectronic devices, photovoltaic cells and semiconductor lasers. Therefore, the effective mass approximation is widely recognized as one of the cornerstones of modern solid-state physics

and semiconductor technology, being extensively researched in fields such as optoelectronic devices and band gap engineering. It should be emphasized that determining the numerical value of the effective mass for different heterostructures is an essential research topic.

The Hamiltonian for the Mathieu quantum dot (MQD) under the influence of the screw dislocation, the external electric field along the radial direction, the external magnetic field and the AB flux field is given by

$$H = \frac{1}{2m^\star}(-i\hbar\vec{\nabla} - e\vec{A})^2 + V_{sd}(r) + V_{MQD}(r) + e_{,}.\mathbf{r}, \tag{4}$$

with $V_{MQD}(r)$ is the Mathieu quantum dot potential, and ξ is the electric field strength. Also, the magnetic field is uniform, and it is applied along the z-axis. Being $\vec{A}$ vector potential, $\vec{A} = \vec{A_1} + \vec{A_2}$, in which $\vec{\nabla} \times \vec{A_1} = \vec{B}$ and $\vec{\nabla} \times \vec{A_2} = 0$ gauge are considered, where $\vec{B} = B\hat{z}$, and $\vec{A_2}$ is the additional magnetic flux Φ_{AB} generated by a solenoid. Components of vector potentials in cylindrical coordinates are given as [54–56]

$$\begin{aligned}
\vec{A_1} &= \left(A_{1r} = 0, A_{1\phi} = Br/2, A_{1z} = 0\right) \\
\vec{A_2} &= \left(A_{2r} = 0, A_{2\phi} = \Phi_{AB}/2\pi r, A_{2z} = 0\right) \\
\vec{A} &= \left(A_r = 0, A_\phi = Br/2 + \Phi_{AB}/2\pi r, A_z = 0\right),
\end{aligned} \tag{5}$$

with Φ_{AB} (the Aharonov–Bohm flux field) and B (the external magnetic field strength). As well as the vector potential arising from the magnetic and AB flux field, the effective vector potential ($\vec{A}_{eff}$) resulting from the screw dislocation is the total effective vector potential of the system as $\vec{A}_{total} = \vec{A_1} + \vec{A_2} + \vec{A}_{eff}$ with

$$\vec{A}_{eff} = \frac{hb}{2\pi r}\frac{\partial}{\partial z}\hat{\phi}. \tag{6}$$

$\vec{A}_{total}$, the deformed potential, the MQD encompassment and the electric field applying in the radial direction constitute the total potential energy for the MQD electrons. For this system, the non-relativistic wave equation is expressed as

$$-\frac{\hbar^2}{2m^\star}\left[\frac{\partial^2}{\partial r^2} + \frac{1}{r}\frac{\partial}{\partial r} + \frac{1}{r^2}(\frac{\partial}{\partial\phi} - \beta\frac{\partial}{\partial z} + \gamma)^2 + \frac{\partial^2}{\partial z^2}\right]\Psi(r,\phi,z)$$

$$+ \left[\frac{ieB\hbar}{2m^\star}(\frac{\partial}{\partial\phi} - \beta\frac{\partial}{\partial z} + \gamma) + \frac{e^2B^2r^2}{8m^\star}\right]\Psi(r,\phi,z)$$

$$+ (V_{sd}(r) + V_{MQD}(r) + e\xi r - E)\Psi(r,\phi,z) = 0, \tag{7}$$

with $\gamma = e\Phi_{AB}/2\pi\hbar$. It should be pointed out that since the external electric field is applied in the radial direction, $\vec{\xi}.\vec{r} = \xi r$. Considering the electron's freedom in the z-direction and 2π period in the azimuthal direction, the following ansatz can be used

$$\Psi(r,\phi,z) = NR(r)e^{im_\ell\phi}e^{ik_zz}, \tag{8}$$

with the normalization constant N, the magnetic quantum number $m_\ell = 0, \pm1, \pm2, \ldots$, and $k_z \exists \Re$. Taking into consideration, the wave function ansatz obtained the following differential equation:

$$R''(r) + \frac{R'(r)}{r} + \left[\frac{2m^\star E}{\hbar^2} + \frac{eB}{\hbar}(m_\ell - \beta k_z + \gamma) - k_z^2 - \frac{e^2B^2}{4\hbar^2}r^2 - \frac{2m^\star}{\hbar^2}e\xi r\right.$$

$$\left. - \frac{(m_\ell - \beta k_z + \gamma)^2 + \frac{b^2}{4\pi^2a^2}(2 + a^2k_z^2)}{r^2} - \frac{2m^\star}{\hbar^2}V_{MQD}(r)\right]R(r) = 0,$$

where the MQD potential is given by

$$V_{MQD}(r) = V_0(\sin^2(\eta r) - \cos(\eta r)), \tag{9}$$

with $V_0 = (1.42 - 1.53x + 0.45x^2)$ eV [18] (being x In−concentration), η (quantum dot potential width parameter). Equation (9) is solved by using Runge–Kutta–Fehlberg (RKF) method. For details of the RKF method, please refer [59, 60].

To specify the NOR, SHG and THG characteristics of the MQD system, it is taken into consideration that monochromatic optical radiation field ($E(t)$) having ω frequency is applied in the radial direction, and is given by

$$\mathbf{E}(t) = \tilde{E}e^{i\omega t} + \tilde{E}e^{-i\omega t}. \tag{10}$$

The time-evolution of the matrix elements of one-electron density operator is stated as [61]

$$\frac{\partial\hat{\rho}_{ij}}{\partial t} = \frac{1}{i\hbar}[\hat{H} - \hat{M}.\mathbf{E}(t), \hat{\rho}]_{ij} - \Gamma_{ij}(\hat{\rho} - \hat{\rho}^{(0)})_{ij}, \tag{11}$$

with $\hat{\rho}$ (density matrix of one-electron system), $\hat{\rho}^{(0)}$ (unperturbed density matrix operator), $\hat{H}_0$ (the Hamiltonian of the system when no electromagnetic field), $\hat{M}.\mathbf{E}(t) = -e\hat{r}E(t)$ (perturbative contribution) and Γ_{ij} (the relaxation rate in damping duration). In order to solve Eq. (11), the following serial solution suggestion can be considered [62]

$$\hat{\rho}(t) = \sum_{n=0}^{\infty} \hat{\rho}^{(n)}. \tag{12}$$

Considering Eq. (12), Eq. (11) is converted to the following form:

$$\frac{\partial \hat{\rho}_{ij}^{(n+1)}}{\partial t} = \frac{1}{i\hbar}\left([\hat{H}, \hat{\rho}^{(n+1)}]_{ij} - i\hbar\Gamma_{ij}\hat{\rho}_{ij}^{(n+1)}\right) - \frac{1}{i\hbar}[e\hat{r}, \hat{\rho}^{(n)}]_{ij}E(t). \tag{13}$$

Due to $E(t)$ optical field, the electronic polarization is expressed as [63]

$$P(t) = (\varepsilon_0\chi_\omega^{(1)}\tilde{E}e^{i\omega t} + \varepsilon_0\chi_0^{(2)}\tilde{E}^2 + \varepsilon_0\chi_{2\omega}^{(2)}\tilde{E}^{(2)}e^{2i\omega t} + \varepsilon_0\chi_\omega^{(3)}\tilde{E}^{(2)}\tilde{E}e^{i\omega t} + \varepsilon_0\chi_{3\omega}^{(3)}\tilde{E}^{(3)}e^{3i\omega t} + \cdots), \tag{14}$$

where ε_0 is the permittivity of free space; $\chi_\omega^{(1)}$, $\chi_0^{(2)}$, $\chi_{2\omega}^{(2)}$ $\chi_\omega^{(3)}$ and $\chi_{3\omega}^{(3)}$ are, respectively, the linear, the optical rectification, the second harmonic generation, the third order and third harmonic generation susceptibilities. By using density matrix approach and iterative method, the NOR, SHG and THG susceptibilities are obtained in the following form [61, 64]:

$$\chi_0^{(2)} = \frac{4e^3\rho_v}{\varepsilon_0\hbar^2}\mu_{01}^2\delta_{01}\frac{\omega_{10}^2(1 + \Gamma_2/\Gamma_1) + (\omega^2 + \Gamma_2^2)(\Gamma_2/\Gamma_1 - 1)}{[(\omega_{10} - \omega)^2 + \Gamma_2^2][(\omega_{10} + \omega)^2 + \Gamma_2^2]}, \tag{15}$$

$$\chi_{2\omega}^{(2)} = \frac{e^3\rho_v}{\varepsilon_0\hbar^2}\frac{\mu_{01}\mu_{12}\mu_{20}}{(\omega - \omega_{10} - i\Gamma_3)(2\omega - \omega_{20} - i\Gamma_3)}, \tag{16}$$
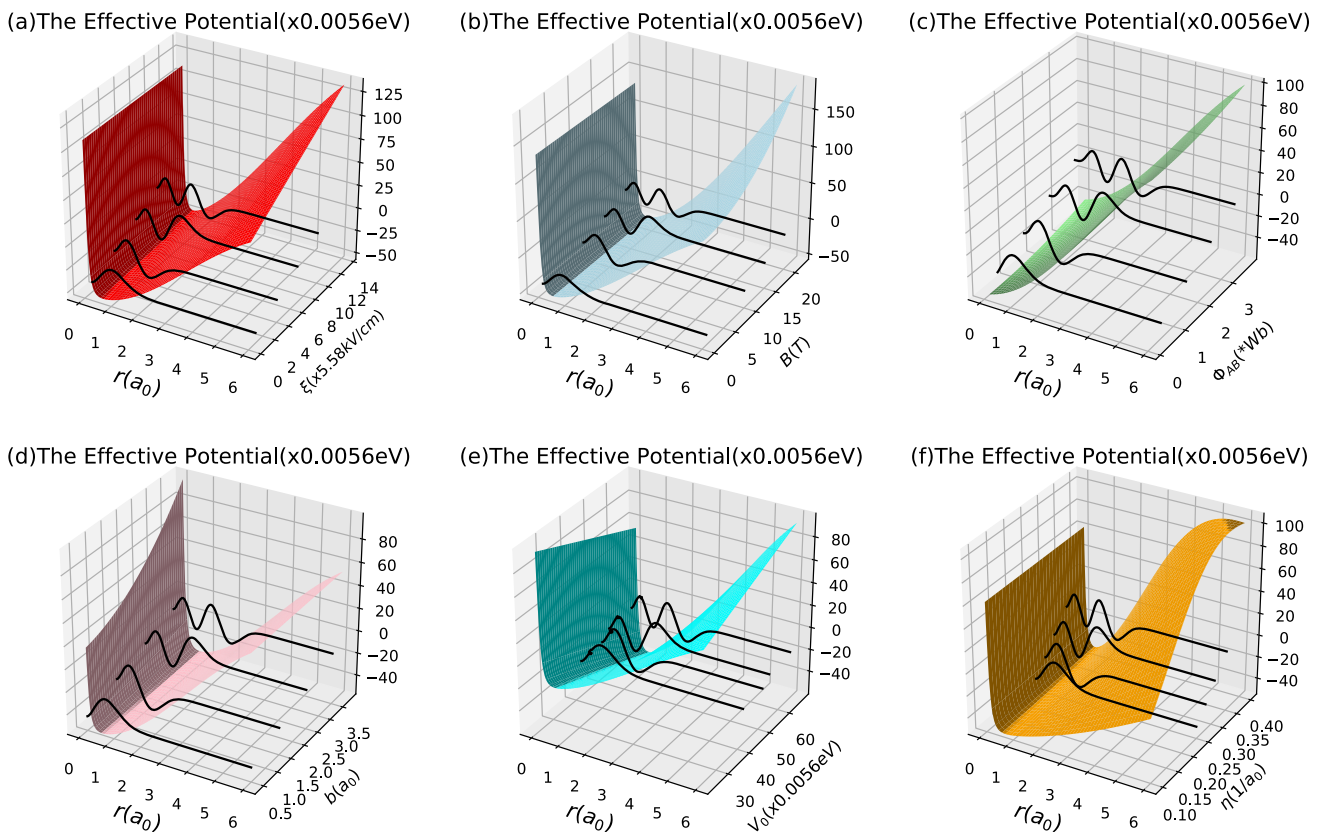

Fig. 2 Plot of the effective potential profile and first four bound state wave functions as function of the radial distance $r(a_0)$ and, **a** the external electric field strength (ξ(kV/cm)), when $B = 0.5$T, $x = 0.4$, $\eta = 0.25/a_0$, $b = 2a$, $\Phi_{AB} = 4.135 \times 10^{-15}$Wb, **b** the external magnetic field strength ($B(T)$), when $F = 30$ kV/cm, $x = 0.4$, $\eta = 0.25/a_0$, $b = 2a$, $\Phi_{AB} = 4.135 \times 10^{-15}$ Wb, **c** the AB flux field strength (Φ_{AB}(Wb)), when $F = 30$ kV/cm, $B = 0.5$ T, $x = 0.4$, $\eta = 0.25/a_0$, $b = 2a$, $\Phi_{AB} = 4.135 \times 10^{-15}$ Wb, **d** the Burgers vector magnitude (b), when $F = 30$ kV/cm, $B = 0.5$ T, $x = 0.4$, $\eta = 0.25/a_0$, $\Phi_{AB} = 4.135 \times 10^{-15}$ Wb, **e** the MQD depth depending on In-concentration (x), when $F = 30$ kV/cm, $B = 0.5$ T, $\eta = 0.25/a_0$, $b = 2a$, $\Phi_{AB} = 4.135 \times 10^{-15}$ Wb, **f** the MQD width parameter ($\eta(1/a_0)$), when $F = 30$ kV/cm, $B = 0.5$ T, $x = 0.4$, $\eta = 0.25/a_0$, $b = 2a$, $\Phi_{AB} = 4.135 \times 10^{-15}$ Wb

$$\chi_{3\omega}^{(3)} = \frac{e^4 \rho_v \mu_{01} \mu_{12} \mu_{23} \mu_{30}}{\varepsilon_0 \hbar^3 (\omega - \omega_{10} - i\Gamma_3)(2\omega - \omega_{20} - i\Gamma_3)} \frac{1}{(3\omega - \omega_{30} - i\Gamma_3)}. \tag{17}$$

where e is the positive electron charge, ρ_v is the electron density, $\omega_{ij} = (E_i - E_j)/\hbar$ is the transition frequency, and $\Gamma_k = 1/T_k$ ($k = 1, 2, 3$) is the damping term related to lifetime of electrons in transition process. $\delta_{01} = |\mu_{00} - \mu_{11}|$ and being ψ_i initial state wave function and ψ_j final state one, $\mu_{ij} = |< \psi_j |r| \psi_i >|$ ($i, j = 0, 1, 2, 3$) is the off-diagonal matrix elements. In consideration of the SHG, THG and NOR characteristic, the numerical setup is taken into account as $m^* = 0.067m_0$ (m_0 is free electron mass), $\rho_v = 3 \times 10^{23}$ m^{-3}, $\varepsilon_{GaAs} = 13.18$, $\varepsilon_0 = 8.854 \times 10^{-12}$ C^2/Nm^2, $\Gamma_{1,2,3} = 1.0$Thz. The quantum dot radius is taken as $R_{dot} = 6a_0$ throughout the study. The effective Rydberg energy and Bohr radius are calculated as $R_y^\star \cong 5.27$MeV and $a_0 = 103.7$Å, respectively [65–67].

3 Result and discussions

We report the effects of the external electric (ξ), magnetic (B) and AB flux fields (ϕ_{AB}) as well as the *In*-concentration (x) and quantum dot width (η) on the NOR, SHG and THG of the In$_x$Ga$_{1-x}$As/GaAs MQD involving in the screw dislocation. Figure 1a presents 3D lattice including the screw dislocation considering the Burger vector along the dislocation line. In Fig. 1b, illustrative screw dislocation in the 3D cylindrical bulk crystal is figured. The respective effective potential and the variation of the wave functions for the first four electronic energy levels are demonstrated as function of radial distance (r), and the electric field (ξ) in Fig. 2a, the magnetic field (B) in Fig. 2b, the AB flux field (ϕ_{AB}) in Fig. 2c, the magnitude of the Burger vector (b) in Fig. 2d, the MQD potential depth (V_0) in Fig. 2e and the MQD width (η) in Fig. 2f.
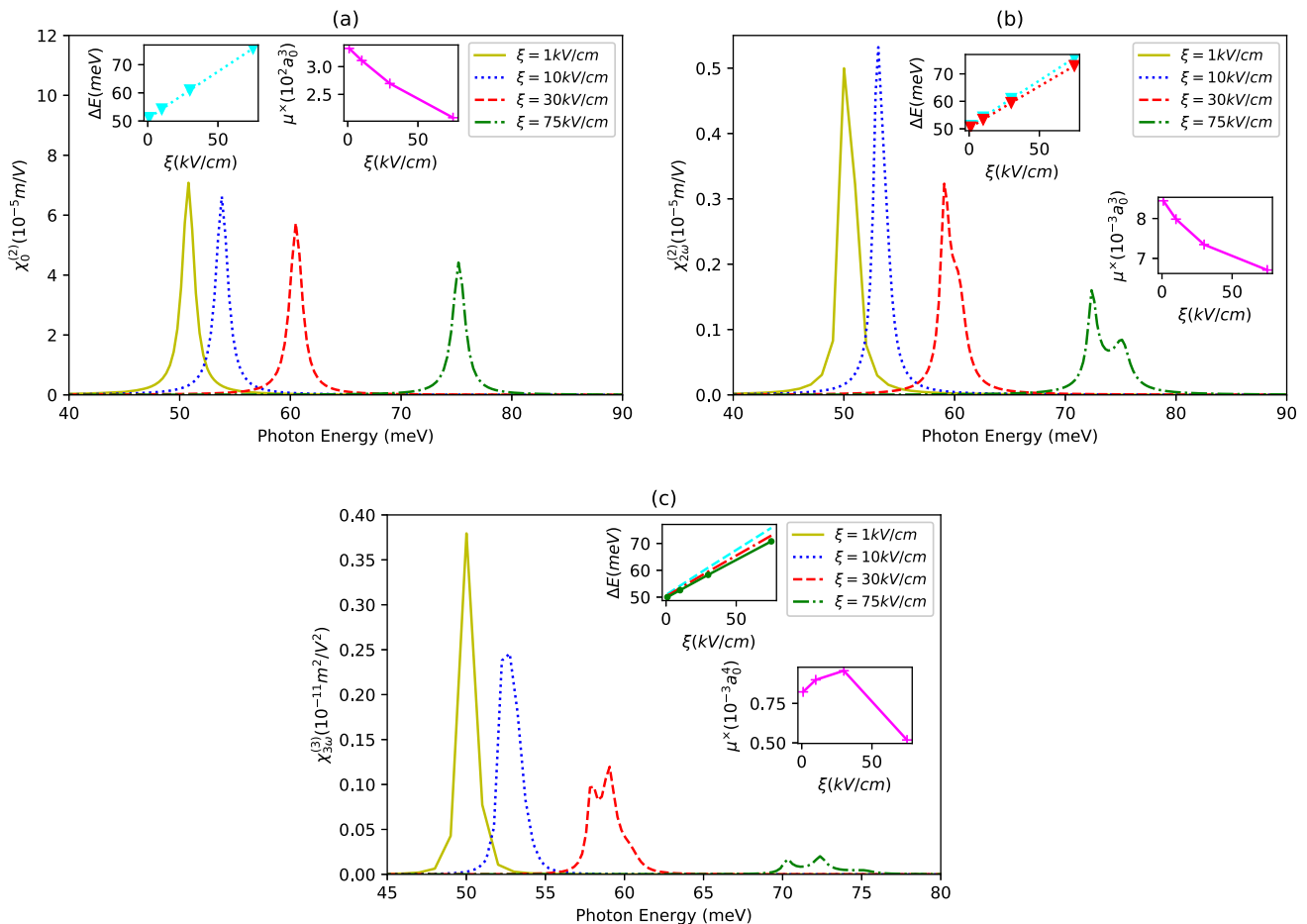
Fig. 3 NOR (**a**), SHG (**b**) and THG coefficients (**c**) of the MQD with $\xi = 1 - 10 - 30 - 75$ kV/cm, $B = 0.5$T, $x = 0.4$, $\eta = 0.25/a_0$, $b = 2a$, $\Phi_{AB} = 4.135 \times 10^{-15}$ Wb. The insets show the relevant energy differences and matrix elements, respectively; as $\Delta E = E_1 - E_0$ (cyan) and $\mu^\times = \mu_{01}^2 \delta_{01}$ for the NOR coefficients (**a**), $\Delta E = (E_2 - E_0)/2$ (red) and $\mu^\times = \mu_{01}\mu_{12}\mu_{20}$ for the SHG coefficients (**b**), $\Delta E = (E_3 - E_0)/3$ (green) and $\mu^\times = \mu_{01}\mu_{12}\mu_{23}\mu_{30}$ for the THG coefficients (**c**)

Figure 3a–c shows the change of the NOR, SHG and THG of the MQD depending on the applied external electric field in consideration of certain constant values of other external fields and the structure parameters, respectively. As the applied external electric field increases, the repulsion of the effective potential increases, as seen in Fig. 2a, which in turn increases the difference between the electron's bound state energy levels. This is confirmed in Fig. 3a inset which shows the change of energy levels depending on the electric field. As can be seen in this inset, the difference between the energy levels ($\Delta E = E_1 - E_0$) increases with the increasing electric field, due to the fact that the applied electric field breaks the symmetry of the structure. Increasing the difference between the energy levels causes the NOR resonant frequencies to be blueshifted. Another remarkable point in Fig. 3a is that the NOR amplitudes decrease due to the increasing electric field. This situation can be explained by the variation of the dipole matrix elements expression depending on the electric field. In Fig. 3a inset, it can be seen that $\mu^{\times} = \mu_{01}^2 \delta_{01}$ decreases as the electric field increases. The dependence of matrix elements ($\mu^{\times} = \mu_{01}^2 \delta_{01}$) on the electric field dominates on the changing of the NOR amplitudes with the electric field. Therefore, as the electric field increases, the NOR amplitudes also decrease (see Fig. 3a). In Fig. 3b, the SHG coefficients are presented depending on the incident photon energy for different values of the applied electric field. The first notable point in the graph is the observation of two distinct resonant peaks of SHG at 2ω. As the electric field value decreases, it is seen that the two peaks formed at the SHG curves turn into a single sharp peak. From this, we can say that as the electric field decreases, the probability of creating frequency dubbing of the structure increases. Also, as the electric field increases, it is seen that the SHG resonant frequencies are blueshifted, which is due to the augment of the difference between the energy levels (ΔE) as a result of the increment in electric field, as can be seen from Fig. 3b inset. The SHG amplitudes decrease with increasing the applied electric field strength. Because, as presented in Fig. 3b inset, the matrix elements statement also decreases with increasing electric field. But, the decrement in the matrix elements statement as result of the increment in the electric field in the weak regimes is not dominant on the SHG amplitudes. Because, in the increment from $\xi = 1$kV/cm to $\xi = 10$kV/cm, despite $\mu^{\times}$ decreases, the SHG amplitude increases. Figure 3c shows the THG coefficients depending on the incident photon energy for different electric field values. Depending on the applied electric field, three different resonant locations are observed at $\xi = 75$kV/cm in the THG resonant peaks. As the electric field increases, the THG character becomes more stable. As shown in Fig. 3c inset, as the electric field increases, ΔE increases, so it is observed in Fig. 3c that the THG resonant frequencies shift to blue. The augment of the applied electric field causes the THG
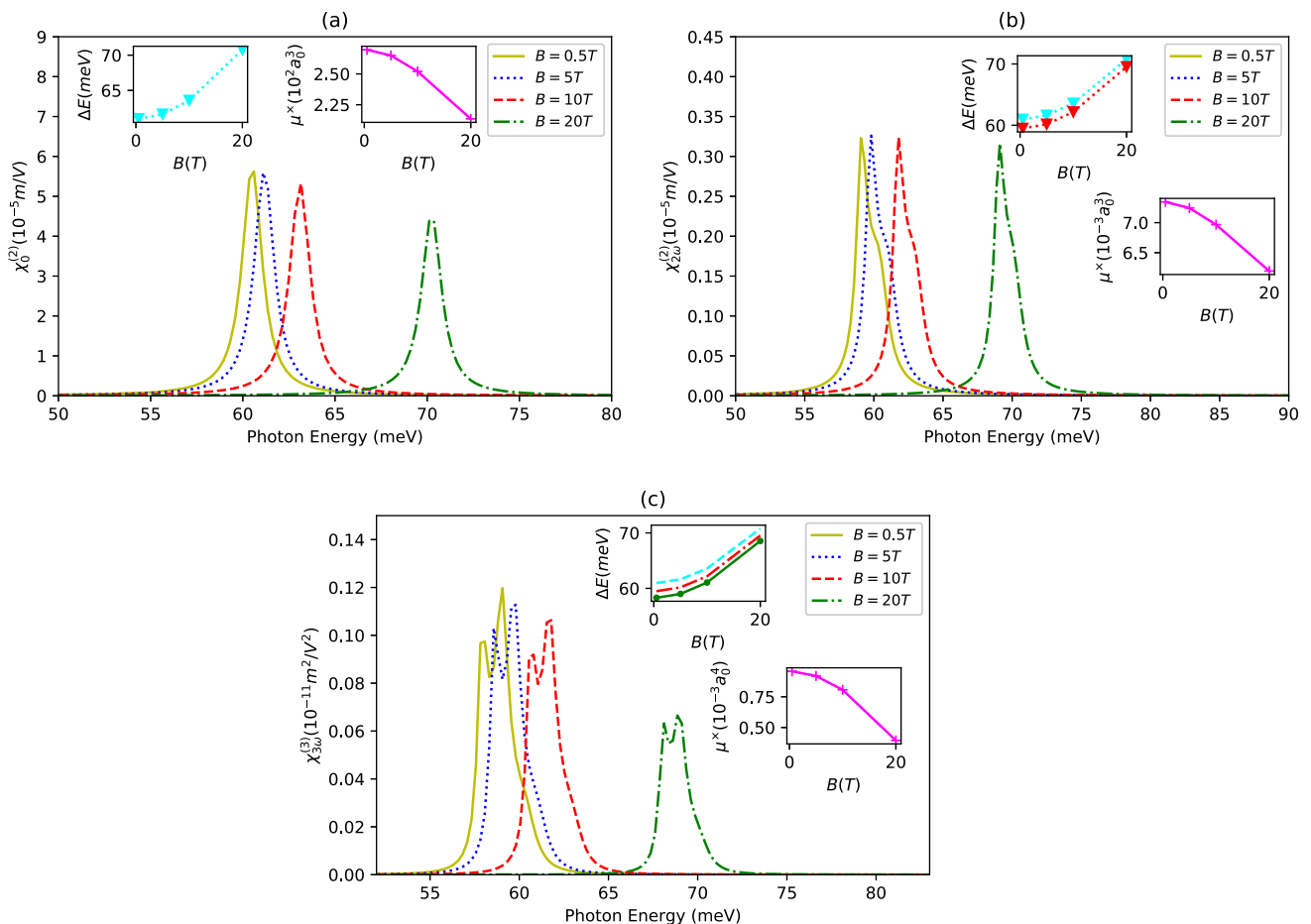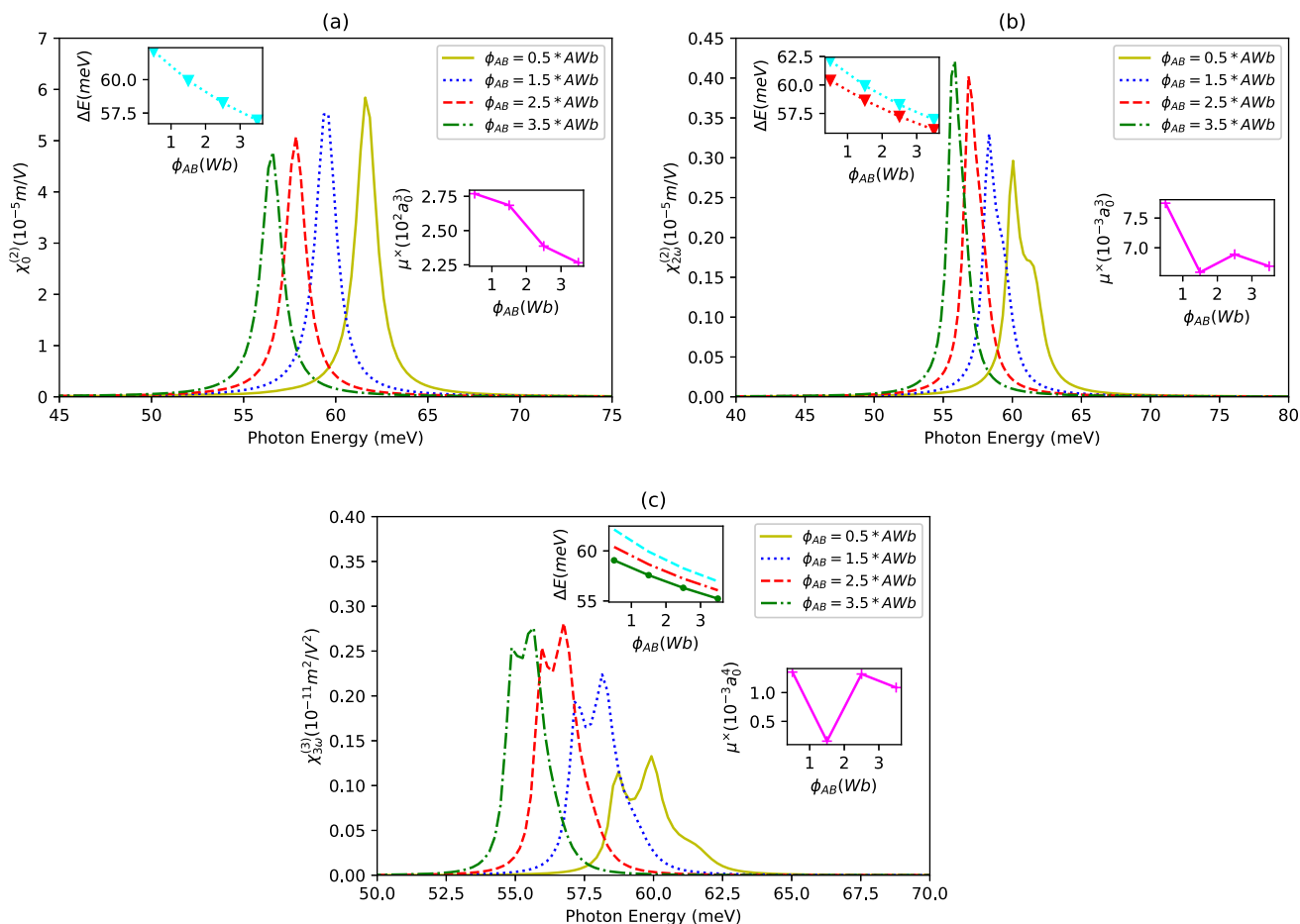

Fig. 4 Same as Fig. 3 but when $\xi = 30$ kV/cm, $B = 0.5 - 5 - 10 - 20$ T, $x = 0.4$, $\eta = 0.25/a_0$, $b = 2a$, $\Phi_{AB} = 4.135 \times 10^{-15}$ Wb

amplitudes to decrease. This reduction is incompatible with the change of the matrix elements expression ($\mu^{\times} = \mu_{01}^2 \delta_{01}$) with the electric field. It can be said that THG resonant amplitudes are influenced not only by the change in matrix elements, but also by the transition frequencies.

In Fig. 4a–c, respectively, the MQD's NOR, SHG and THG characters are presented as a function of incident photon energy for different external magnetic field values. In Fig. 4a, it is seen that the NOR resonant frequencies shift to blue as the magnetic field increases because the repulsion of the MQD increases with the increasing magnetic field, which can be seen from the change of the effective potential profile in Fig. 2b. This causes the difference between electronic energy levels to increase, as can be clearly seen in Fig. 4a inset. Another important point observed in the graph is that the NOR amplitudes decrease as the magnetic field increases (see Fig. 4a inset). As can be seen, the amplitudes lower due to the decrease in the matrix elements statement ($\mu^{\times}$) with increasing magnetic field. When studying the change in SHG, similar to the interpretations made in the NOR graphs, it can be observed from the inset in Fig. 4b that the blueshift of the SHG resonant frequencies is due to the increase in energy difference with the magnetic field. In Fig. 4b inset, it is seen that the matrix elements expression ($\mu^{\times}$) decreases as the magnetic field increases. However, in Fig. 4b, it is observed that the SHG amplitudes are almost unchanged with increasing magnetic field. Then, it can be said that the matrix elements are not dominant over the SHG amplitudes. Considering Eq.(16), it is clear that the SHG amplitudes change with a form in which both the matrix elements and resonant frequencies are active. On the other hand, the SHG character tends to be more stable as the magnetic field increases. Because the small peak is getting smoother. In Fig. 4c, it is seen that as the magnetic field increases, the THG resonant frequencies shift to blue, as in the NOR and SHG because as presented in Fig. 2b, the repulsiveness of the potential increases as the magnetic field increases, and in this case, the energy difference (ΔE) between localizations increases (see Fig. 4c). However, the THG amplitudes decrease with increasing magnetic field. This decrease in amplitudes is consistent with the variation of dipole matrix elements with respect to the magnetic field because the dipole matrix elements expression also decreases with increasing magnetic field.

In Fig. 5a–c, respectively, the NOR, SHG and THG characters of the MQD are presented as a function of incident photon energy for different AB flux field values. It is seen in Fig. 5a that the NOR resonant frequencies redshift as the AB flux field strength
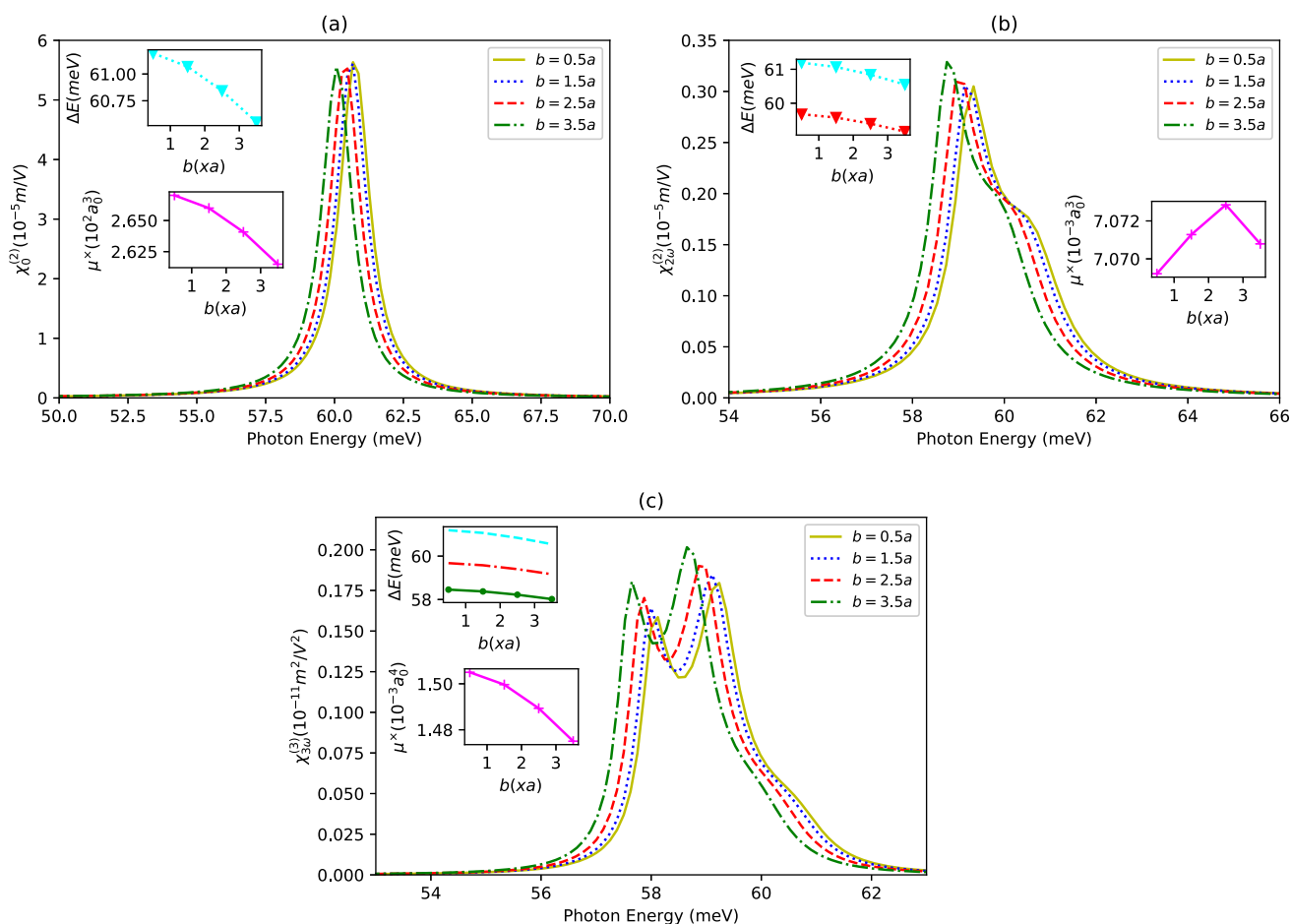

Fig. 5 Same as Fig. 3 but when $\xi = 30$ kV/cm, $B = 0.5$ T, $x = 0.4$, $\eta = 0.25/a_0$, $b = 2a$, $\Phi_{AB} = (0.5 - 1.5 - 2.5 3.5) \times 4.135 \times 10^{-15}$ Wb, $A = 4.135 \times 10^{-15}$

increases because the depth of the effective potential profile decreases with increasing AB flux field, but its width increases (see Fig. 2b). This change reduces the difference between electronic energy levels, which causes the resonant frequencies to redshift (see Fig. 5a). It is important to note that the NOR amplitudes decrease as the AB flux field increases, the reason of which is the decrement in the matrix elements expression ($\mu^{\times}$) with increasing AB flux field (see Fig. 5a). The SHG resonant frequencies redshift as the AB flux field increases, similar to the NOR frequencies (see Fig. 5b). As mentioned before, this is due to the reduction in the energy difference, as can be clearly seen in Fig. 5b inset, in line with the effective potential change in Fig. 2b. Another remarkable point is that the SHG amplitudes increase as the AB flux field increases. As seen in Fig. 5b inset, the matrix elements ($\mu^{\times}$) behave as decreasing–increasing–decreasing versus increasing AB flux field values; however, the SHG amplitudes enhance constantly. From this, it can be stated that not only the matrix elements, but also the transition frequencies play a dominant role in the SHG amplitudes. It is important to note that the mathematical form responsible for the variation of resonant amplitudes with both matrix elements and transition frequencies is not known, but it can be determined using numerical methods. As the AB flux field increases, the smaller SHG resonant peak smoothens out and eventually a more stable SHG character is formed. Then, it can be said that as the AB flux field increases, the probability of frequency dubbing of the structure becomes stronger. In Fig. 5c, it can be observed that an increase in AB flux field causes a redshift in the THG resonant frequencies, which is primarily due to the same mechanism as in NOR and SHG. Similar to the SHG character, reducing the value of the AB flux field in THG smooths out the smaller resonant amplitude, leading to a more stable THG character. There is no direct relationship between the amplitude behavior and the matrix elements (see Fig. 5c inset). Therefore, it would not be accurate to attribute the effect solely to the matrix elements or the specified mathematical form of the matrix elements on the resonant amplitudes.

In Fig. 6a–c, respectively, the NOR, SHG, and THG characteristics of MQD are presented as a function of the incident photon energy for different magnitudes of screw dislocation. In Fig. 6a, a very faint redshift in the NOR resonant frequencies is observed as a result of accreted screw dislocation (the increment of b), which is a decrement in the effective potential interaction's strength due to accreted dislocation (Fig. 2d). Correspondingly, the difference between electronic energy levels decreases monotonically with the increase of b and a feeble redshift is observed. The matrix elements ($\mu^{\times}$) decrease slightly depending on increasing screw dislocation (see Fig. 6a). When analyzing with respect to b the change of the SHG coefficients in Fig. 6b and THG coefficients in

Fig. 6 Same as Fig. 3 but when $\xi = 30$ kV/cm, $B = 0.5$ T, $x = 0.4$, $\eta = 0.25/a_0$, $b = 0.5 - 1.5 - 2. - 3.5a$, $\Phi_{AB} = 4.135 \times 10^{-15}$ Wb

Fig. 6c, it is seen that the SHG and THG resonant frequencies shift to red similar to the change in the NOR. The reason for these changes is the decrease in energy difference ΔE with increasing b, as shown in the Fig. 6b, c inset. As observed in the SHG panel, the corresponding matrix element exhibits an aggressive change, while in the THG panel, a monotonic decrease is observed. Therefore, it is evident that the expression of matrix elements alone does not dominate the change in SHG and THG resonant amplitudes.

In Fig. 7a–c, respectively, the NOR, SHG and THG characters are introduced for different values of *In*-concentration (x) of the MQD having the screw dislocation as a function of incident photon energy. As can be clearly seen in Fig. 2e, as x increases, the effective potential strength enhances. In this case, the energy difference between the bound state localizations also increases (see Fig. 7a inset), resulting in a blueshift of the NOR resonant frequencies. Also, the NOR amplitudes decrease as the value of x increases in accordance with the change of the matrix elements in Fig. 7b inset. In Fig. 7b, when examining the change of the SHG coefficients depending on the *In*-concentration (x), it is seen that as x increases, the SHG resonant peaks shift to blue and the resonant amplitudes decrease, in line with the augment in the energy difference and the decrement in the matrix elements. In Fig. 7c, it is seen that as x increases, similar to the NOR and SHG resonant frequencies, the THG resonant frequencies shift to blue and the relevant amplitudes decrease, in which reason is as in the NOR and SHG characters.

In Fig. 8a–c, respectively, the MQD's the NOR, SHG and THG are given as a function of incident photon energy for different η values. As seen in Fig. 8a, as η increases, the NOR resonant frequencies shift to blue, while the resonant amplitudes decrease. Because, in Fig. 2e, it is seen that as the value of η increases, the repulsion of the effective potential increases, which is the main factor of the blueshifting. As can be seen in Fig. 8a, the NOR amplitudes decrease correspondingly as the matrix elements ($\mu^\times$) decrease with increasing η value. When the change of SHG coefficients in Fig. 8b and THG coefficients in Fig. 8c is analyzed according to η, it is evident that the SHG and THG resonant frequencies blueshift, similar to the change in the NOR. The reason for these changes is also the potential repulsion and the increase in the difference between the electronic levels. Also, it is seen that the SHG and THG resonant amplitudes decrease as η increases (see Fig. 8b, c), for which it is clear that the behavior of matrix elements expression is dominant.
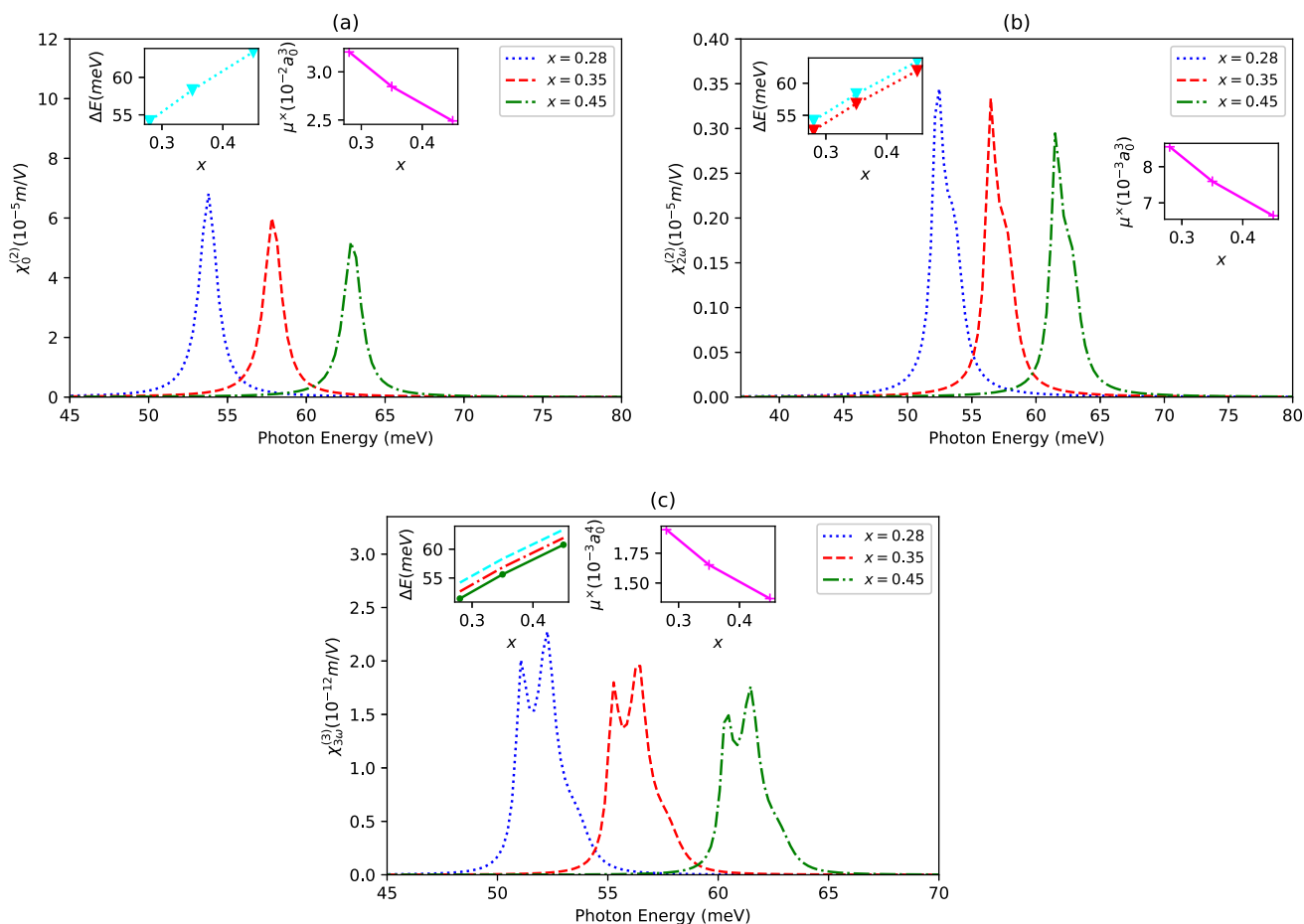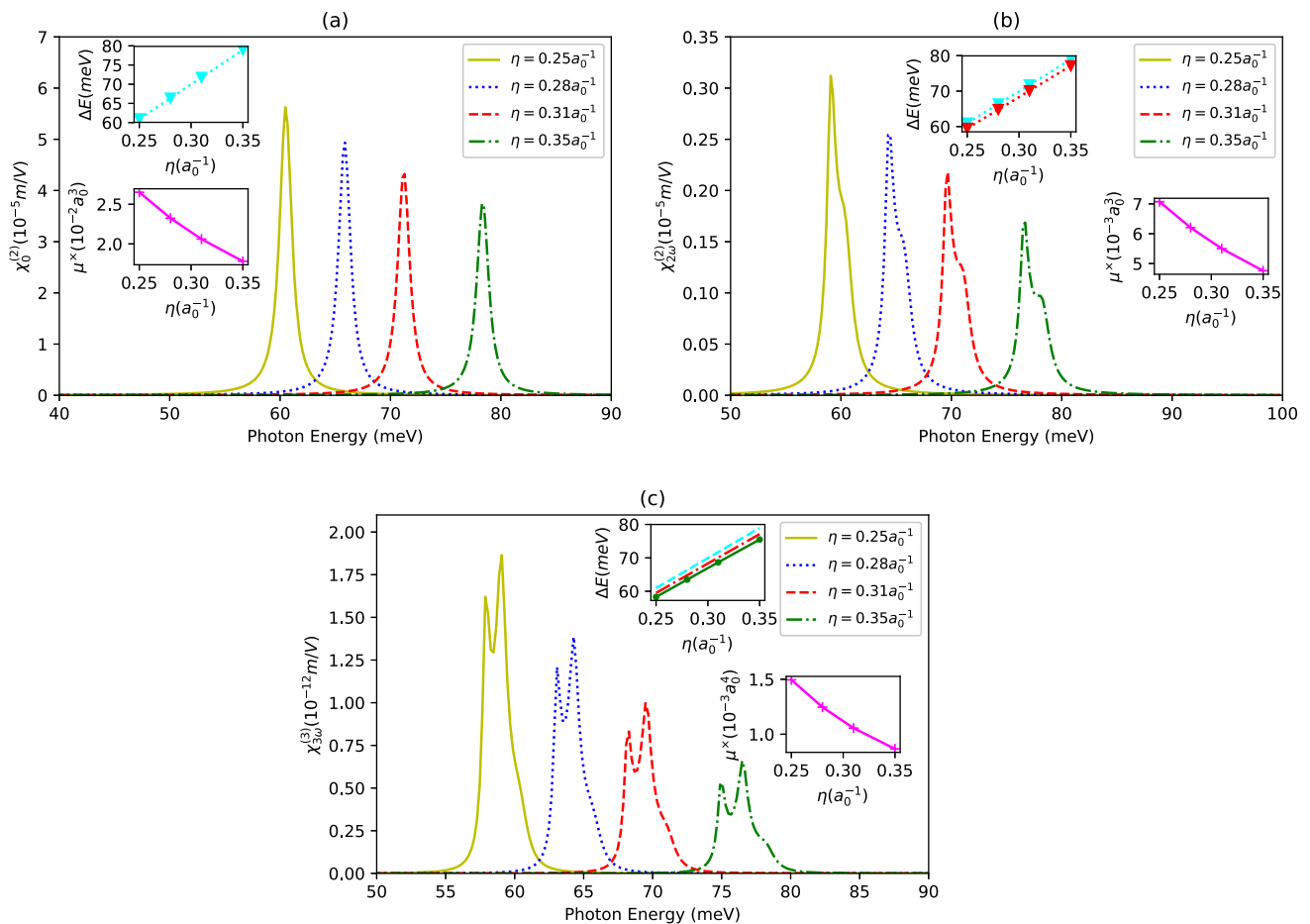

Fig. 7 Same as Fig. 3 but when $\xi = 30$ kV/cm, $B = 0.5$ T, $x = 0.28 - 0.35 - 0.45$, $\eta = 0.25/a_0$, $b = 2a$, $\Phi_{AB} = 4.135 \times 10^{-15}$ Wb

Fig. 8 Same as Fig. 3 but when $\xi = 30$ kV/cm, $B = 0.5$ T, $x = 0.4$, $\eta = 0.25 - 0.28 - 0.31 - 0.35/a_0$, $b = 2a$, $\Phi_{AB} = 4.135 \times 10^{-15}$ Wb

4 Concluding remarks

In this study, the nonlinear optical properties of the MQD with screw dislocation have been extensively investigated, taking into account the changes in structural parameters under the influence of external electric fields, magnetic fields and Aharonov–Bohm flux fields. The defect of screw dislocation in the MQD has been studied not only by itself, but also in conjunction with external electric fields, external magnetic fields, and AB flux field because the strain energy induced by the screw dislocation is an inhibitory factor that prevents the formation of bound states in a structure alone. The applied external magnetic field creates an additional parabolic confinement effect, thereby enhancing the confinement effect on the electron. Both external fields and structural parameters are influential in the optical responses of the structure. The determination of the functional ranges of these parameters through theoretically calculated effects will provide useful advantages for optoelectronic devices obtained experimentally. The applied external electric and magnetic fields serve as alternatives to the structural parameters in terms of optimality and resonant frequencies. Moreover, in terms of resonant frequencies, the AB flux field and screw dislocation are alternatives to each other.

Availability of data and materials This manuscript has no associated data added to any data repository. The datasets generated during and/or analyzed during the current study are available from the corresponding author on reasonable request.

Code availability Not applicable.

Declarations

Conflict of interest The authors report no conflict of interest.

References

1. T. Chakraborty, *Quantum Dots: A Survey of the Properties of Artificial Atoms* (Elsevier, Amsterdam, 1999), p. 254
2. J.Y. Marzin, J.M. Gerard, A. Izrael, D. Barrier, G. Bastard, Photoluminescence of single InAs quantum dots obtained by self-organized growth on GaAs. Phys. Rev. Lett. **73**, 716 (1994)
3. R. Pozner, E. Lifshitz, U. Peskin, Triple quantum dot based nano-electromechanical memory device. Appl. Phys. Lett. **107**, 113109 (2015)
4. D. Loss, D.P. DiVincenzo, Quantum computation with quantum dots. Phys. Rev. A **57**, 120 (1998)
5. Y.S. Park, J. Roh, B.T. Diroll, R.D. Schaller, V.I. Klimov, Colloidal quantum dot lasers. Nat. Rev. Mater. **6**, 382 (2021)
6. R. Schaller, V. Klimov, High efficiency carrier multiplication in PbSe nanocrystals: implications for solar energy conversion. Phys. Rev. Lett. **92**, 186601 (2004)
7. Y.M. Huang, K.J. Singh, A.C. Liu, C.C. Lin, Z. Chen, K. Wang, Y. Lin, Z. Liu, T. Wu, H.C. Kuo, Advances in quantum-dot-based displays. Nanomaterials **10**, 1327 (2020)
8. C. Cheng, Q. Liang, M. Yan, Z. Liu, Q. He, T. Wu, S. Luo, Y. Pan, C. Zhao, Y. Liu, Advances in preparation, mechanism and applications of graphene quantum dots/semiconductor composite photocatalysts: a review. J. Hazard. Mater. **424**, 127721 (2022)
9. S. Coe-Sullivan, J.S. Steckel, W.K. Woo, M.G. Bawendi, V. Bulovic, Large-area ordered quantum-dot monolayers via phase separation during spin-casting. Adv. Funct. Mater. **15**, 1117 (2005)
10. P.A. Franken, A.E. Hill, C.W. Peters, G. Weinreich, Generation of optical harmonics. Phys. Rev. Lett. **7**, 118 (1961)
11. R.W. Boyd, *Nonlinear Optics* (Academic Press, Boston, 1992)
12. B. Rui-Xue, W. Jue-Han, W. Da-Hai, W. Zhong-Ming, Research progress of low-dimensional semiconductor materials in field of nonlinear optics. Acta Phys. Sin. **69**, 184211 (2020)
13. P. Hosseinpour, A. SoltaniVala, J. Barvestani, Effect of impurity on the absorption of a parabolic quantum dot with including Rashba spin-orbit interaction. Physica E Low-Dimens. Syst. Nanostruct. **80**, 48 (2016)
14. Q. Zhao, S. Aqiqi, J.F. You, M. Kria, K.X. Guo, E. Feddi, Z.H. Zhang, J.H. Yuan, Influence of position-dependent effective mass on the nonlinear optical properties in $Al_xGa_{1-x}As$/GaAs single and double triangular quantum wells. Physica E **115**, 113707 (2020)
15. A. Boda, B. Boyacioglu, U. Erkaslan, Dia- and paramagnetism and total susceptibility of GaAs quantum dots with Gaussian confinement. Phys. E Low-Dimens. Syst. Nanostruct. **44**, 1826 (2012)
16. J.H. Davies, *The Physics of Low-Dimensional Semiconductors: An Introduction*, 5th edn. (Cambridge University Press, Cambridge, 1999)
17. E. Mathieu, Memoire sur Le Mouvement Vibratoire d'une Membrane de forme Elliptique. Journl de Mathematiques Pures et Appliquees **13**, 137 (1868)
18. S. Adachi, *Physical Properties of III–V Semiconductor Compounds. A Wiley-Interscience Publication* (Wiley, New York, 1992)
19. F. Klopf, J.P. Reithmaier, A. Forchel, Highly efficient GaInAs/(Al)GaAs quantum-dot lasers based on a single active layer versus 980 nm high-power quantum-well lasers. Appl. Phys. Lett. **77**, 1419 (2000)
20. I. Lagraa, B. Soudini, H. Abid, S. Taleb, Study and optimization of structure InAs/InGaAs quantum dot in-a-well long-wave infrared photodetector. Optik **251**, 168494 (2022)
21. Y. Nambu, S. Takahashi, K. Yoshino, A. Tanaka, M. Fujiwara, M. Sasaki, A. Tajima, S. Yorozu, A. Tomita, Efficient and low-noise single-photon avalanche photodiode for 1.244-GHz clocked quantum key distribution. Opt. Express **19**, 20531 (2011)
22. N. Namekata, H. Takesue, T. Honjo, Y. Tokura, S. Inoue, High-rate quantum key distribution over 100 km using ultra-low-noise, 2-GHz sinusoidally gated InGaAs/InP avalanche photodiodes. Opt. Express **19**, 10632 (2011)
23. F. Chancerel, P. Regreny, J. L. Leclercq, M. Volatier, A. Jaouad, M. Darnon, S. Fafard, M. Gendry, V. Aimez, Comparison of Various InGaAs-based Solar Cells for Concentrated Photovoltaics Applications, HAL Id: hal-03407479 (2021)
24. J.H. Tsai, High-performance AlInAs/GaInAs -doped HEMT with negative differential resistance switch for logic application. Solid-State Electron. **48**, 81 (2004)
25. Y. Aharonov, D. Bohm, Significance of electromagnetic potentials in quantum theory. Phys. Rev. **115**, 485 (1959)
26. M. Brooks, Seven wonders of the quantum world. New Sci. (2010)
27. E.N. Bogachek, U. Landman, Aharonov–Bohm oscillations, and thermodynamic and spectral properties in a two-dimensional electron gas with an antidot. Phys. Rev. B **52**, 14067 (1995)
28. S.M. Ikhdair, B.J. Falaye, M. Hamzavi, Nonrelativistic molecular models under external magnetic and AB flux fields. Ann. Phys. **353**, 298 (2015)
29. C. Filgueiras, M. Rojas, G. Aciole, E.O. Silva, Landau quantization, Aharonov–Bohm effect and two-dimensional pseudoharmonic quantum dot around a screw dislocation. Phys. Lett. A **380**, 3847 (2016)
30. I.J. Njoku, C.P. Onyenegecha, C.J. Okereke, E. Omugbe, Relativistic bound states of the pseudoharmonic potential in the presence of external magnetic and Aharonov–Bohm fields. Eur. Phys. J. Plus **137**, 842 (2022)
31. H.V. Phuc, Magnetic and Aharonov–Bohm flux fields effects on two-photon absorption properties in cylindrical quantum dot. SSRN 4225791 (2022)
32. Y. Murakami, K. Nagai, A. Koga, Efficient Control of High Harmonic Generation in Carbon Nanotubes using the Aharonov–Bohm Effect, Mesoscale and Nanoscale Physics (cond-mat.mes-hall), 1 (2023)
33. M. Khosravi, B. Vaseghi, K. Abbasi, G. Rezaei, Magnetic susceptibility of cylindrical quantum dot with Aharonov–Bohm flux: simultaneous effects of pressure, temperature, and magnetic field. J. Superconduct. Nov. Magn. **33**, 761 (2020)
34. B. Aalu, Intersubband optical absorption in Gaussian GaAs quantum dot in the presence of magnetic, electrical and AB flux fields. Physica B **575**, 411699 (2019)
35. E. Ribeiro, A.O. Govorov, W. Carvalho Jr., G. Medeiros-Ribeiro, Phys. Rev. Lett. **92**, 126402 (2004)
36. D. Bejan, C. Stan, Aharonov–Bohm effect in pseudo-elliptic quantum rings: influence of geometry, eccentricity and electric field. Eur. Phys. J. Plus **134**, 1 (2019)
37. C. Filgueiras, E.O. Silva, 2DEG on a cylindrical shell with a screw dislocation. Phys. Lett. A **379**, 2110 (2015)
38. M.K. Bahar, F. Ungan, Magneto-optical specifications of Rosen-Morse quantum dot with screw dislocation. Int. J. Quantum Chem. **120**, 1 (2020)
39. J.K. Mackenzie, E.H. Sondheimer, The theory of the change in the conductivity of metals produced by cold work. Phys. Rev. **77**, 264 (1950)
40. S.C. Hunter, F.R.N. Nabarro, The propagation of electrons in a strained metallic lattice. Proc. R. Soc. A Math. Phys. Sci. **220**, 542 (1953)
41. R. Landauer, Conductivity of cold-worked metals. Phys. Rev. **82**, 520 (1951)
42. D.L. Dexter, Scattering of electrons in metals by dislocations. Phys. Rev. **86**, 770 (1952)
43. J.R. Huang, T.W. Chen, J.W. Lee, C.F. Huang, L.S. Hong, A perspective on leakage current induced by threading dislocations in 4H-SiC Schottky barrier diodes. Mater. Lett. **310**, 131506 (2022)
44. J.H. You, H.T. Johnsona, Effect of screw dislocation density on optical properties in n-type wurtzite GaN. J. Appl. Phys. **101**, 023516 (2007)
45. N. Soheibi, M. Hamzavi, M. Eshghi, S.M. Ikhdair, Screw dislocation and external fields effects on the Kratzer pseudo dot. Eur. Phys. J. B **90**, 212 (2017)

46. Z.H. Zhang, J.H. Yuan, Electronic and nonlinear optical properties in AlGaAs/GaAs Gaussian confinement quantum dot under applied electric field. Physica E **147**, 115594 (2023)
47. N. Amin, A. JohnPeter, Structure dependent third order nonlinear susceptibility in the presence of impurity and magnetic field in CdS/ZnS core/shell quantum dot. Phys. B Condens. Matter **625**, 413477 (2022)
48. M. Sayraç, Effects of applied external fields on the nonlinear optical rectification, second, and third-harmonic generation in an asymmetrical semi exponential quantum well. Opt. Quant. Electron. **54**, 1 (2022)
49. S.G. Kosion, E. Paspalakis, Nonlinear optical response of a strongly-driven quantum dot exciton–biexciton system. Micro Nanostruct. **175**, 207508 (2023)
50. M.O. Katanaev, I.V. Volovich, Theory of defects in solids and three-dimensional gravity. Ann. Phys. **216**, 1 (1992)
51. R. Bausch, R. Schmitz, L.A. Turski, Single-particle quantum states in a crystal with topological defects. Phys. Rev. Lett. **80**, 2257 (1998)
52. H. Taira, H. Shima, Optical conductivity of semiconductor crystals with a screw dislocation. Solid State Commun. **177**, 61 (2014)
53. R. Bausch, R. Schmitz, U.A. Turski, Quantum motion of electrons in topologically distorted crystals. Ann. Phys. **8**, 181 (1999)
54. E.N. Bogacheki, U. Landman, Edge states, Aharonov–Bohm oscillations, and thermodynamic and spectral properties in a two-dimensional electron gas with an antidot. Phys. Rev. B **52**, 14067 (1995)
55. A. Cetin, A quantum pseudodot system with a two- dimensional pseudoharmonic potential. Phys. Lett. A **372**, 3852 (2008)
56. S.M. Ikhdair, M. Hamzavi, R. Sever, Spectra of cylindrical quantum dots: the effect of electrical and magnetic fields together with AB flux field. Physics B **407**, 4523 (2012)
57. F. Meng, A.M. Stephan, A. Forticaux, S. Jin, Screw dislocation driven growth of nanomaterials. Acc. Chem. Res. **46**, 1616 (2013)
58. A.A. Lima, F.M. Filgueiras, Torsion effects on condensed matter: like a magnetic field but not so much. Eur. Phys. J. B **90**, 1 (2017)
59. K. Kılıç, M.K. Bahar, Optical response of plasma processed quantum dot under the external fields. Int. J. Quantum Chem. **121**, 1 (2021)
60. C.C. Steven, P.C. Raymond, *Numerical Methods for Engineers* (McGraw-Hill, New York, 1990)
61. Y.B. Yu, H.J. Wang, Third-harmonic generation in two-dimensional pseudo-dot system with an applied magnetic field. Superlattices Microstruct. **50**, 252 (2011)
62. E. Rosencher, Model system for optical nonlinearities: asymmetric quantum wells. Phys. Rev. B **252**, 44 (1991)
63. G. Rezaei, B. Vaseghi, F. Taghizadeh, M.R.K. Vahdani, M.J. Karimi, Intersubband optical absorption coefficient changes and refractive index changes in a two-dimensional quantum pseudodot system. Superlattices Microstruct. **48**, 450 (2010)
64. R.W. Boyd, *Nonlinear Optics*, 3rd edn. (Rochester, New York, 2007)
65. S. Paul, J.B. Roy, P.K. Basu, Empirical expressions for the alloy composition and temperature dependence of the band gap and intrinsic carrier density in $Ga_x In_{1x}$As. J. Appl. Phys. **69**, 827 (1991)
66. F. Ungan, M.K. Bahar, M.G. Barseghyan, L.M. Perez, D. Laroze, Effect of intense laser and electric fields on nonlinear optical properties of cylindrical quantum dot with Morse potential. Optik **236**, 16662 (2021)
67. P. Başer, M.K. Bahar, Evaluation of the external electric- and magnetic field-driven Mathieu quantum dot's optical observables. Physica B **639**, 413991 (2022)